Journal of South American Earth Sciences 31 (2011) 214–226

Contents lists available at ScienceDirect

Journal of South American Earth Sciences

journal homepage: www.elsevier.com/locate/jsames

Variability of atmospheric precipitable water in northern Chile: Impacts on interpretation of InSAR data for earthquake modeling

D. Remy [a,*], M. Falvey [b], S. Bonvalot [a], M. Chlieh [c], G. Gabalda [a], J.-L. Froger [d], D. Legrand [b]

[a] GET (UMR CNRS/IRD/UT3 UMR5563 UR234) Obs. Midi Pyrénée, 14 av. E. Belin, 31400 Toulouse, France
[b] Departamento de Geofisica, Facultad de Ciencias Físicas y Matemáticas, Universidad de Chile – Blanco Encalada 2002, Santiago, Chile
[c] Institut de Recherche pour le Développement (IRD), GeoAzur (Université de Nice-CNRS-IRD-OCA), Bât 4, 250 rue Albert Einstein, Sophia Antipolis, 06560 Valbonne, France
[d] LMV (UBP-CNRS-IRD), Obs. de Physique du Globe de Clermont-Ferrand, 5 rue Kessler, 63038 Clermont-Ferrand Cedex, France

ARTICLE INFO

Article history:
Received 22 February 2010
Accepted 17 January 2011

Keywords:
Interferometry
Earthquake modeling
Deformation
Troposphere
Northern Chile

ABSTRACT

The use of Synthetic Aperture Radar interferometry (InSAR) in northern Chile, one of the most seismically active regions in the world, is of great importance. InSAR enables geodesists not only to accurately measure Earth's motions but also to improve fault slip map resolution and our knowledge of the time evolution of the earthquake cycle processes. Fault slip mapping is critical to better understand the mechanical behavior of seismogenic zones and has fundamental implications for assessing hazards associated with megathrust earthquakes. However, numerous sources of errors can significantly affect the accuracy of the geophysical parameters deduced by InSAR. Among them, atmospheric phase delays caused by changes in the distribution of water vapor can lead to biased model parameter estimates and/or to difficulties in interpreting deformation events captured with InSAR. The hyper-arid climate of northern Chile might suggest that differential delays are of a minor importance for the application of InSAR techniques. Based on GPS, Moderate Resolution Imaging Spectroradiometer (MODIS) data our analysis shows that differential phase delays have typical amplitudes of about 20 mm and may exceptionally exceed 100 mm and then may impact the inferences of fault slip for even a Mw 8 earthquakes at 10% level. In this work, procedures for mitigating atmospheric effects in InSAR data using simultaneous MODIS time series are evaluated. We show that atmospheric filtering combined with stacking methods are particularly well suited to minimize atmospheric contamination in InSAR imaging and significantly reduce the impact of atmospheric delay on the determination of fundamental earthquake parameters.

1. Introduction

Northern Chile (18°–26°S) is located above the convergent inter-plate contact between the Nazca and South American plates (Fig. 1), one of the most seismically active regions in the world. Monitoring of ground deformation in this region is of great importance as it can provide new insights into the seismic deformation cycle in the Andean margin (Ruegg et al., 1996; Delouis et al., 1997; Klotz et al., 1999; Pritchard et al., 2002; Perfettini et al., 2005; Pritchard and Simons, 2006). The hyper-arid climate of northern Chile, that hosts the 'Atacama Desert', one of the driest deserts on Earth, makes it an ideal setting for the application of InSAR techniques because surface features change little between image acquisitions. Consequently, numerous studies conducted along the central Andean margin have been published in recent years, illustrating the unique capabilities of InSAR to reveal the patterns of crustal deformation related to the earthquake cycle (Chlieh et al., 2004; Pritchard and Simons, 2006). The desert environment might suggest that the errors introduced by water vapor delay are of a minor importance in northern Chile. However, despite the fact that rainfall has never been recorded in some parts of the Atacama Desert, water vapor is abundant in the atmosphere above the region, and exhibits a high spatio-temporal variability (Falvey and Garraud, 2005). Consequently, phase signals related with differential path delays between two acquisition dates are likely to be produced in observed interferograms with comparable ranges of amplitude and wavelength as those produced by geodynamical processes. This may lead to misinterpretation of the subtle crustal deformation signals that occur during the seismic cycle. Various studies already analyzed the tropospheric signal on InSAR in other part of the world and several approaches for minimizing atmospheric contaminations in InSAR measurements have been proposed (Delacourt et al., 1998; Beauducel et al., 2000; Hanssen, 2001; Remy et al., 2003; Cavalié et al., 2007, 2008;

* Corresponding author. Tel.: +33 (0)5 61 33 26 69; fax: +33 (0)5 61 33 25 60.
E-mail address: remy@lmtg.obs-mip.fr (D. Remy).

0895-9811/$ – see front matter © 2011 Elsevier Ltd. All rights reserved.
doi:10.1016/j.jsames.2011.01.003

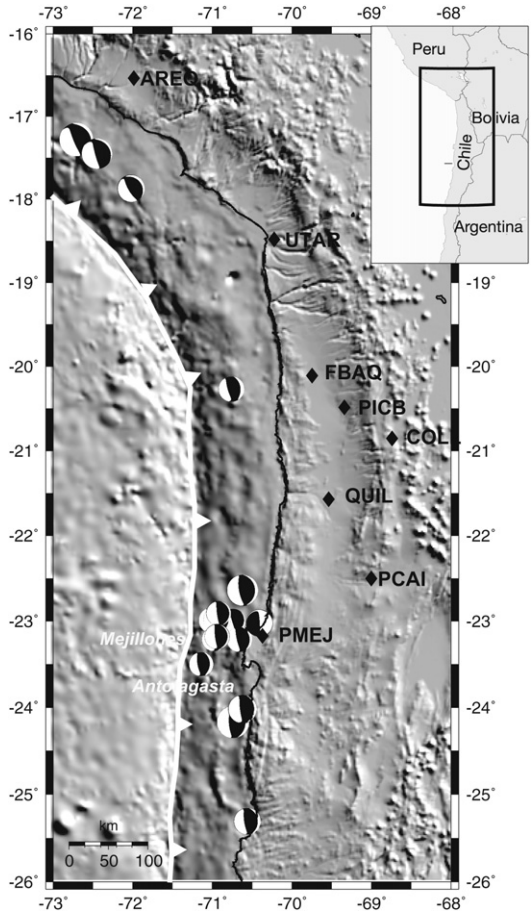

Fig. 1. Tectonic setting of the northern Chile subduction zone. The white barbed line in the ocean indicates the trench location. The focal mechanisms of subduction earthquakes with Mw > 6 are from Harvard Centroid Moment Tensor Catalog for the period 1992–2009. The black diamonds represent the location of the permanent GPS stations used in this study.

Puysségur et al., 2007; Doin et al., 2009). The relatively recent advent of satellite based solar spectrometers providing high resolution spatial imagery of Precipitable Water Vapor (PWV) has allowed the SAR community to progress forward in analyzing such atmospheric effects in interferograms (e.g.,Li et al., 2003; Li, 2004; Pavez et al., 2006; Froger et al., 2007; Puysségur et al., 2007; Loveless and Pritchard, 2008).

The aim of this paper is to evaluate the impact of atmospheric errors on interpretation of InSAR data for earthquake modeling and on the accuracy of the fault slip map deduced from InSAR. This study is based primarily of a 12-month database of twice daily PWV images from the MODIS solar spectrometer, along with hourly GPS estimates of PWV from eight semi-permanent stations (Fig. 1). First, we address in some detail the quality of MODIS PWV estimates by comparison with GPS estimates of PWV. From these estimates, we carefully examine the character of atmospheric water vapor variability in northern Chile and evaluate its probable impact on InSAR imaging done in northern Chile. We focus next on the impact of atmospheric water vapor variability on the determination of fundamental source parameters for one of the largest subduction earthquake registered in this area: the Mw 8.1 Antofagasta earthquake of July 30, 1995. Finally, we evaluate the efficiency of alternative approaches for mitigating atmospheric effects based on the use of multi-image information in order to improve the earthquake modeling.

2. Data acquisition and processing

2.1. MODIS derived PWV measurements

The MODIS instrument is a satellite based imaging spectrometer with channels in the solar reflective spectral range. It is installed aboard NASA's TERRA and AQUA satellites, and has 36 channels operating between visible and long wave infrared (0.4–14.4 μm) wavelengths. The two satellites orbit the Earth in sun-synchronous near polar trajectories, which generally pass over the Northern Chile twice per day at approximately 03h00' and 15h00' UTC (TERRA) and 06h30' and 18h30' UTC (AQUA). The MODIS instrument allows estimation of the PWV based on water vapor attenuation of solar radiation reflected from the surface in the near-infrared (NIR) channels (Gao and Kaufman, 2003). The PWV may only be estimated during the daytime over areas where there is a reflective surface in the NIR band, that is, over land areas, cloud tops and bodies of water where solar reflection ('sun glint') is high. Atmospheric water vapor transmittances are estimated using ratios of water vapor absorbing channels and atmospheric 'window' (non-absorbing) channels. The ratios partially remove the effects of variation of surface reflectance with wavelength. PWV is then derived from the transmittances based on theoretical radiative transfer calculations. Systematic errors in NIR-PWV may arise from un-modeled surface reflectivity variability and absorption due to haze. Validation studies of MODIS PWV have shown one-sigma accuracy of about 1.6–1.7 mm (Bennartz and Fischer, 2001).

PWV images are made along a swath 2330 km wide, with a spatial resolution of 1 km at nadir. The most important solar spectrometer dataset used in this study is based on the MODIS 'Joint' data product, which contains PWV estimates re-sampled onto a 5-km resolution grid to reduce the size of the image files. We obtained all available images for the Northern Chile and Southern Peru (15°S–25°S) over the period November 13, 2003 until December 15, 2004: 1964 images in total. We applied stringent quality control measures to remove all potentially unreliable PWV estimates. In particular, image pixels flagged as unreliable include those where clouds were detected, where the resolution was lower than 10 km (i.e, pixels near to the edges of the image swath), or which were over water surfaces.

2.2. GPS derived PWV measurements

The GPS data are provided by 7 permanent and semi-permanent stations of the geodetic monitoring network of North Chile installed jointly by Institut de Physique du Globe de Paris (IPGP), Institut de Recherche pour le Développement (IRD) and University of Chile (Fig. 1), in the frame of the French–Chilean cooperation program. We also use GPS data from a permanent station of the International GNSS Service (IGS) in Arequipa, Peru (AREQ). All stations are equipped with geodetic dual frequency GPS receivers recording at a sampling rate of 30 s. Detailed site and instrumentation information may be found on websites of University of Chile (http://ssn.dgf.uchile.cl/) and SOPAC (http://sopac.ucsd.edu), respectively. All available GPS data were batch processed in daily sessions using the GAMIT/GLOBK software (Herring et al., 2006a,, 2006b) for the period 13 November 2003 until 15 December 2004. Several IGS stations throughout South America were included in the processing, ensuring a well defined reference frame and the long baselines necessary to retrieve absolute PWV (Tregoning et al., 1998). The total zenith delay was modeled from the computed daily GPS solutions as a piecewise linear process with knots at 2 h intervals.

To convert GPS zenith delay estimates to PWV the standard method first outlined in Bevis et al. (1996) was used. This methodology uses an observation of the surface pressure at the GPS site to

remove the hydrostatic component of the total delay (*Zh*). The remaining wet component of delay is then converted to PWV based on an estimate of the moisture weighted mean atmospheric temperature (*Tm*), most often obtained from a surface temperature observation (Bevis et al., 1994). Numerous validation studies in many climates have shown that GPS PWV estimates made in this way have absolute uncertainties of around 1–2 mm (Li et al., 2003). The GPS instruments used in this study were generally not equipped with, or located near to, permanent meteorological instrumentation. In order to obtain estimates of the surface pressure necessary for removal of *Zh*, data from the National Center for Environmental Protection–National Center for Atmospheric Research (NCEP–NCAR) meteorological Reanalysis were interpolated to the station locations. Comparison of reanalyzed surface pressure with observations at synoptic sites in the region (not shown) indicates random errors of ±1 hPa (rms) and long term bias of less than 2 hPa, which correspond to errors in the estimated PW of less than 0.3 and 0.6 mm, respectively. The parameter *Tm* was also calculated using Reanalysis, a methodology that is in fact recommended over the use of surface temperature observations (Bevis et al., 1994).

3. Results of PWV data analysis

3.1. Meteorological characteristics of the study area

It is useful to begin with some preliminary comments on the major geographical and climatological factors that govern the spatial distribution of water vapor in northern Chile. The region is widely referred to as the 'Atacama Desert', one of the driest deserts on Earth, and several geo-climatic factors conspire to produce its particular, hyper-arid climate (e.g., Rutllant et al., 2003). The most important of these is the high altitude Andes mountain chain that runs along the eastern edge of the desert, and the South Pacific anticyclone: a semi-permanent zone of high pressure situated over the ocean to the west of coast. The former prevents moist continental air to the east of the Andes from reaching the Atacama Desert. The latter produces a region of large scale subsidence and drying. Over the coastal region and Pacific Ocean to the west, a shallow (~1000 m) Marine Boundary Layer (MBL), often capped by a thin layer of stratocumulus cloud, is almost always present. While strong evaporation over the ocean means the MBL is relatively moist, the presence of a steep escarpment along the coast of northern Chile usually prevents the moist air mass from entering the elevated desert.

These climatic features are identifiable in data derived from the MODIS imagery. Fig. 2a shows the mean cloud cover (CC) (i.e., frequency of pixels flagged as cloudy) derived from the MODIS image database. The stratocumulus cloud deck can be identified as the area of frequent (>50%) cloud occurrence over the ocean to the west of Chile and Peru. The clear skies above the Atacama are indicated by substantially lower values of cloud cover frequency, especially in the south of the study area, where the CC is about 10%. The CC increases somewhat to the north, and with altitude, being higher along the western rim of the Cordillera due to the occurrence of summertime convection (e.g., Garreaud, 1999). Fig. 2b shows the mean PWV derived from full MODIS image database. The most significant cause of variation in the PWV field is the topography, which can vary over 5000 m over spatial scales of 50 km or so. The highest PWV values are concentrated along a thin coastal strip where the land surface is below the top of the moist MBL.

3.2. Comparison of MODIS and GPS estimates of PWV

The quality of the MODIS PWV estimates is now evaluated by comparison with GPS estimates at each of the 7 stations in the study area (Fig. 1). For each MODIS PWV image the data pixels closest to the GPS stations were extracted. Assuming that the pixel passed the quality control tests mentioned in Section 2.2, the time series of two-hourly GPS estimations was interpolated linearly to obtain the GPS PWV at the time of the MODIS overpass.

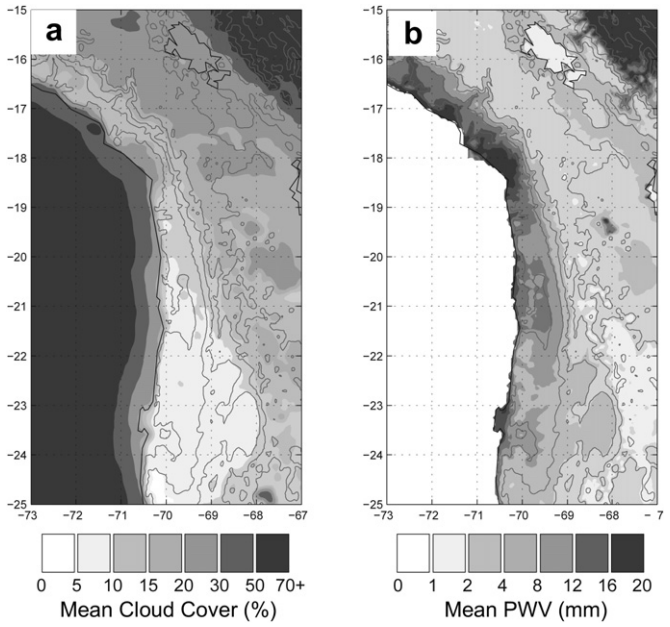

Fig. 2. a) Mean cloud fraction and b) Mean precipitable water vapor in the northern Chile region as determined by MODIS observations over the period 15 November 2002–15 December 2004.

The number of paired PWV estimates that could be formed in this way varies considerably from station to station (Table 1), mainly due to gaps in the GPS data series. Geographical variations in MODIS ground coverage and cloudiness had a much smaller effect on data availability. Note that the reduction of resolution from 1 km to 5 km in the MODIS 'Joint' data product we used (as mentioned in 2.1) should not greatly affect the results of the comparison with GPS, as the effective spatial resolution of GPS PWV is considerably lower than 5 km.

Time-series and scatter plots of the GPS and MODIS PWV are shown in Fig. 3 for three representative GPS sites encompassing the studied area from sea level to the cordillera: PMEJ, AREQ and COLL (shown in Fig. 1). A very good temporal comparison is seen in all cases, with similar seasonal and higher frequency (weather related) variations reproduced in both time series. This is reflected in the scatter plots at each station, which show strong linear relationships between the GPS and MODIS PWV estimates. The MODIS PWV is

Table 1
Comparison of GPS and MODIS Precipitable Water Vapor (PWV). N is the number of paired PWV estimates, which vary mainly due to missing GPS data. *a* and *b* refer to the results of a linear fit between GPS and MODIS PWV of the form $PWV_{MOD} = b \times PWV_{GPS} + a$. Sigma is the standard error of the linear relation (i.e., the variance of the residuals) and r is the correlation coefficient. All bracketed values are the estimated uncertainties of the corresponding parameters.

GPS Station	Height (m)	N	b	a (mm)	σ (mm)
PMEJ	63	244	1.13 (0.02)	−3.52(0.42)	1.76 (0.11)
UTAR	103	82	1.13 (0.02)	−2.57(0.67)	2.15 (0.17)
FBAQ	1114	219	1.03 (0.02)	−2.50(0.19)	1.19 (0.08)
QUIL	1225	109	1.00 (0.04)	−1.46(0.38)	1.36 (0.13)
PICB	1391	79	0.98 (0.02)	−1.62(0.26)	0.90 (0.10)
PCAL	2316	92	1.03 (0.02)	−4.83(0.27)	0.80 (0.08)
AREQ	2504	248	0.98 (0.01)	−3.81(0.21)	1.14 (0.07)
COLL	3914	89	0.72 (0.07)	−1.67(0.36)	0.75 (0.08)

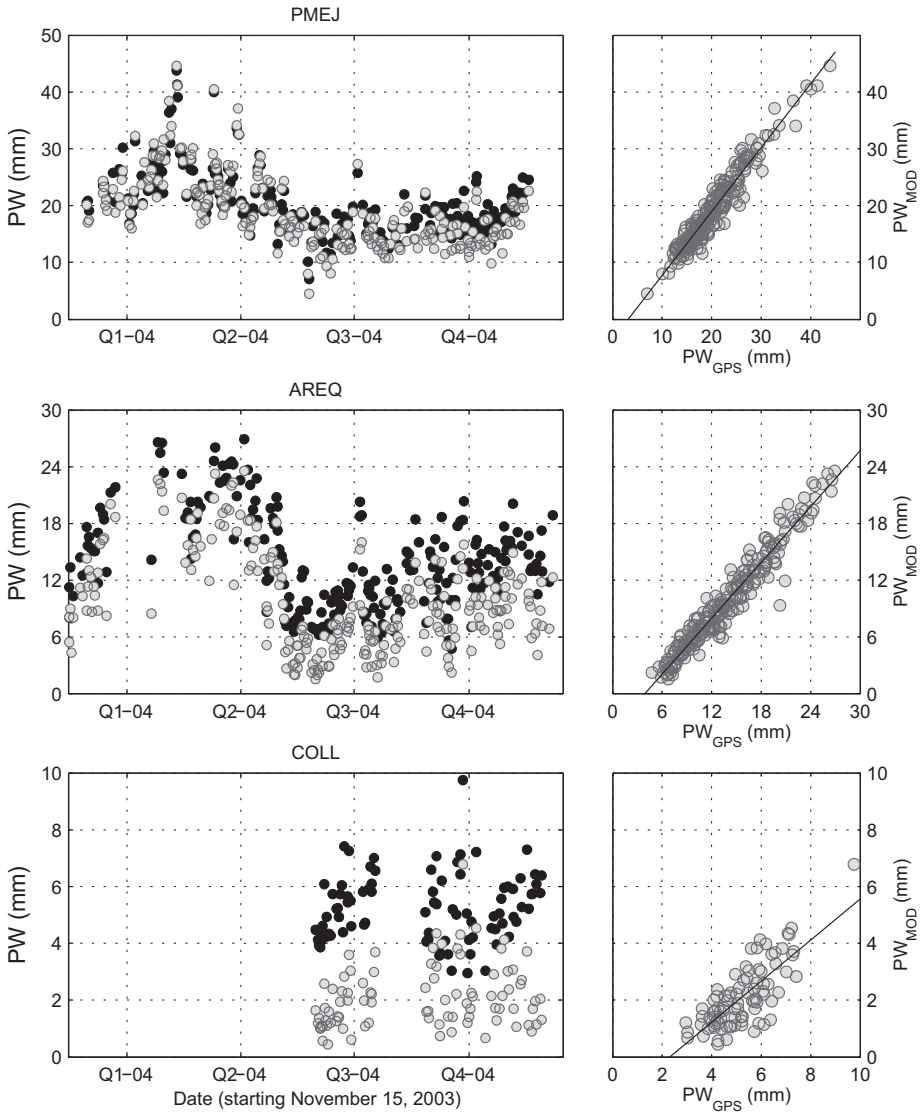

Fig. 3. Comparison of GPS and MODIS PWV at three selected sites: PMEJ (Mejillones Peninsula, 63 m), AREQ (Arequipa, 2504 m) and COLL (Colina, 3914 m). The panel on the left shows GPS time series (black) and MODIS PWV estimates (gray) between the 15 November 2002 and 15 December 2004. The right panels show scatter plots of all paired observations at each site with the 'best fit' linear regression.

consistently lower than the GPS PWV at all three sites, indicative of biases in at least one of the two observing systems.

The statistical results presented in Table 1 summarize comparison between GPS and MODIS PWV at all GPS stations derived from a standard linear least squares fit the form: $PWV_{MOD} + \sigma = a + b^{*}PWV_{GPS}$ which finds the values of zero point offset (a), and scaling factor (b) parameters that minimize the standard deviation of the residual vector ($<\sigma>$). Ideal values of a, b and $<\sigma>$ are 0, 1 and 0 respectively.

The standard deviations ($<\sigma>$) vary between 0.75 and 2 mm, with a mean value of 1.3 mm, which compares well to similar statistics that have been presented in previously published comparisons of MODIS and GPS PWV (e.g., Li et al., 2003). The $<\sigma>$ exhibits a tendency to be highest at moister, low-lying sites, a trend that can be made clear by plotting variation of $<\sigma>$ with the mean PWV at each site (Fig. 4). We find $<\sigma>$ can be well modeled as the sum of a constant 'base-line' random error ($\sigma 0$) and a relative error (σr) whose value is proportional to the PWV (i.e, $\sigma r = \kappa$ PWV). Optimal values for $\sigma 0$ and κ are found to be 0.5 and 0.05 (i.e., 50% and 5%) respectively. It is not possible to determine to what extents MODIS and GPS contribute to the error terms. Both may be expected to have some degree of constant and relative errors.

At most GPS stations (FBAQ, QUIL, PICB, PCAL and AREQ) the scaling factors (b) are identical to one (95% confidence). The exceptions are the coastal stations PMEJ (63 m a.s.l) and UTAR (103 m a.s.l), which both have high b parameters of 1.13; and COLL (3914 m a.s.l), where b is low at 0.72. As these stations are at the low and high altitude extremes of the GPS network, it may be that the b parameter has some altitude dependence. Given the presence of a negative bias in the MODIS PWV retrievals, values of $b < 0$ are to be expected at high altitude points such as COLL, because the zero bounded MODIS PWV retrieval algorithm must damp the variability of low PWV values. This problem is expected to occur at locations where the mean PWV approaches the bias in the MODIS estimates. As discussed in more detail in Li et al. (2003) the presence of a scaling error in MODIS data parameters will leave a residual error in corrected interferograms if the MODIS images are left uncalibrated, and an altitude or other dependency of this error will further complicate the situation. This error could be substantial. For example, the value of b of $\sim$0.7 at the COLL site indicates that in

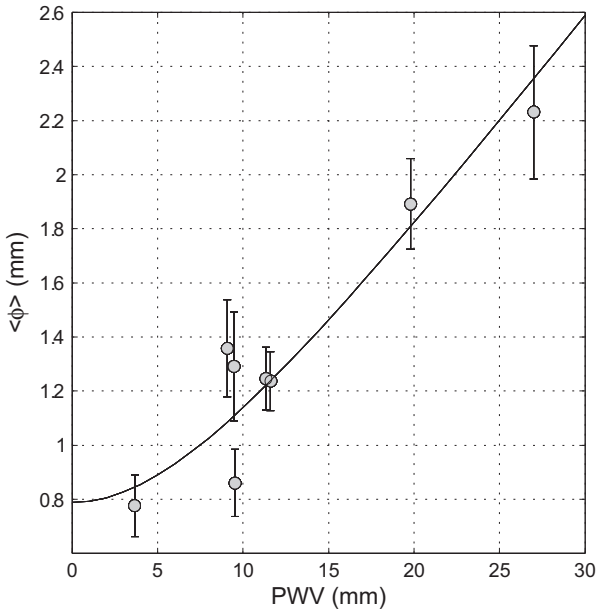

Fig. 4. Standard deviation of the residual $<\sigma>$ of the linear fit between PWV_{mod} and PWV_{GPS} is plotted against the mean PWV at each GPS site. The solid line shows the best fit curve of a simple model for $<\sigma>$ as the sum of a constant and relative error, i.e, $<\sigma>^2 = \sigma_0^2 + (\kappa PWV)^2$, where σ_0 and κ are 0.5 and 0.05, respectively.

extreme cases, the atmospheric phase difference between low and high altitude points obtained from MODIS could be overestimated by as much as 30%. Such extreme case arise for interferograms that are constructed from one image under very dry (low PWV) conditions and another very moist (high PWV) conditions. Given the limited data available in this study we cannot offer any altitude based correction scheme, and a better sampling at high and low altitudes will be necessary to pursue this subject further. Nonetheless, the good results ($b = 1$) obtained over large area for the majority of stations indicate that between altitudes of 1000 m and 2500 m no external calibration of MODIS data is necessary.

Large negative biases (the *a* parameters from Table 1), between −1.6 and −3.5 are found at all stations, with no clear pattern in their spatial variability. The biases are considerably larger than those that have generally been found in GPS validation studies, suggesting that the MODIS data have a tendency to underestimate PWV over Atacama region, perhaps due to an unusually high reflectivity of its desert surface. For the purpose of InSAR processing, biases of this sort are of minor importance because the time constant errors tend to cancel when forming an interferogram (i.e., the difference of phase measurements between two different Single Look Complex (SLC) images).

3.3. Evaluation of water vapor effects on SAR interferograms

In this section we examine the likely magnitude of atmospheric effects on SAR imagery in the Atacama region using the now validated database of MODIS PWV. For the demonstrative purpose of this study, and in order to better match with the horizontal dimension of SAR images, we focus on a relatively small section (~300 km × 300 km), of the overall study area, roughly centered between Mejillones peninsula and the Salar of Atacama. This area being also the site of the last magnitude 8 earthquake that occurred in the studied area (Antofagasta, Mw 8.1; July 30, 1995), as discussed later in this paper.

The two-way SAR slant path signal delay (SPD) induced by atmospheric water vapor may be given by (Zebker et al., 1997):

$$\mathrm{SPD} = \frac{\mathrm{PWV}}{\Pi \cos\theta_{\mathrm{inc}}} \quad (1)$$

where the SPD is expressed in mm, PWV is the precipitable water vapor (mm) and θ_{inc} is the incidence angle of the SAR radar beam. π is an atmospheric parameter that depends on the meteorological profile of pressure, temperature and moisture along the radar beam path (Bevis et al., 1996). However, since the variability of π is generally more than an order of magnitude lower that of the PWV, to a first approximation π may be treated as a constant with a value of about 0.15. Since the phase of an interferogram is the difference of phase between two different SAR images, the slant path delay phase difference (ΔSPD) is given by:

$$\Delta\mathrm{SPD} = \frac{(\mathrm{PWV}_{t1} - \mathrm{PWV}_{t2})}{\Pi \cos\theta_{\mathrm{inc}}} \quad (2)$$

where ΔSPD is in mm, and PWV_{t1} and PWV_{t2} are the precipitable water vapor (mm) at the observation times t1 and t2, respectively. This equation shows that what matters to an interferogram is the change in distribution of PWV from scene to scene rather than the absolute value of PWV for a particular scene.

From the original database of MODIS images, we selected all those which were more than 85% complete coverage over the study area. A total of 300 images were retained. We used a Monte Carlo approach for simulating interferometric phase screens from random combinations of 300 MODIS images. From the original pool, we formed a large set of 1000 randomly selected image pairs. For each image pair, we computed the PWV difference ($PWV_{t1} - PWV_{t2}$) between the two acquisitions and we related it to the predicted slant phase delay (ΔSPD) using the Eq. (2), assuming a nominal mean incidence angle (θ_{inc}) of 23° corresponding to the ERS and ENVISAT (swath 2) satellites. At a given pixel the ΔSPD is evaluated with respect to an arbitrary chosen reference point located in the Salar of Atacama (68°17'W, 23°17'S). Fig. 5a and b show maps of the median and 95% percentiles of ΔSPD. The median may be interpreted as representing the level of atmospheric signal in a 'typical' (most probable) interferogram. The 95% percentiles may be interpreted as 'bad luck' cases when atmospheric contamination is unusually large but nonetheless plausible. These maps give a good indication of the expected tropospheric noise in interferograms computed over the study area. They reveal that the amplitude of atmospheric phase delay in ERS or ENVISAT (swath 2) radar Line-of-Sight (LOS) usually reaches about 20–30 mm between the coast and the Salar de Atacama reference point in the median value cases (Fig. 5a) and may be as high as 100 mm in the 95% percentiles cases (Fig. 5b). Along the coast the spatial gradients in ΔSPD are highest, reaching the equivalent of 2 fringes in C-band interferograms, which puts significant limitations on the measurement of subtle crustal deformations in single interferograms.

In most image pairs, ΔSPD varies strongly with topography. Fig. 6 illustrates a typical example of ΔSPD as function of the elevation data extracted from a pair of MODIS images. The strong altitude dependence of ΔSPD is the basis for one of the traditional approaches to mitigate atmospheric effects in interferograms which consists to estimate the topographic dependence of the interferometric phase (Beauducel et al., 2000; Chlieh, 2003; Remy et al., 2003; Peyrat et al., 2006; Pritchard and Simons, 2006). Using this approach one assumes that the atmosphere over a given area is approximately horizontally homogenous and ΔSPD is modeled as a monotonically decreasing or increasing function of surface altitude. Nevertheless, this method has a disadvantage in that any geodynamical signals correlated with topography in the same way will also be removed. Another problem is that the deformation is not always localized, but can extend across the entire image or the entire area with good coherence (see Fig. 7 for instance). In this case it may be difficult to

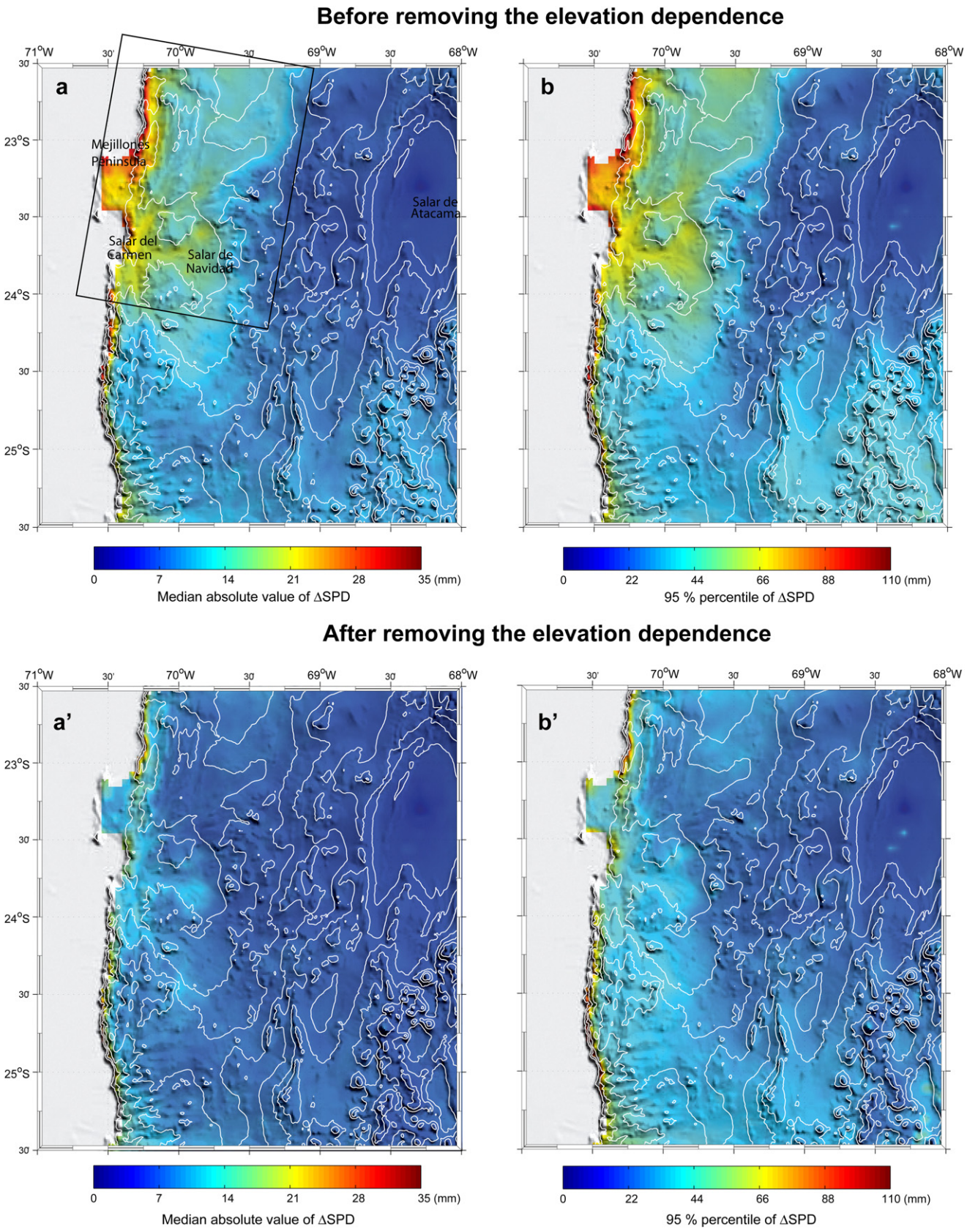

Fig. 5. Median absolute value of the ΔSPD with respect to a reference point located on Salar de Atacama taken from 1000 member Monte Carlo sample of random image pairs from a pool of 300 nearly complete MODIS images and their 95% confidence intervals. The black box in a) places the location of the interferograms composed from images taken on the descending satellite track 96 shown in Fig. 7). a) Median absolute value of the ΔSPD without removing the elevation dependence. Note the fine scale ΔSPD patterns, which are observed along the coast in particularly on the Mejillones Peninsula and on the Salar del Carmen and the salar de Navidad. b) The upper 95% percentile of the ΔSPD distribution indicating high atmospheric contamination. a' and b' are the median absolute value of ΔSPD after removing the elevation dependence using a generalized spline approximation from the ΔSPD field map shown in a and the corresponding upper 95% percentile of the ΔSPD distribution. Note the different color scale change between a–a' and b–b' to emphasize difference. The elevation of the study area is represented by white contour lines at 500-m intervals.

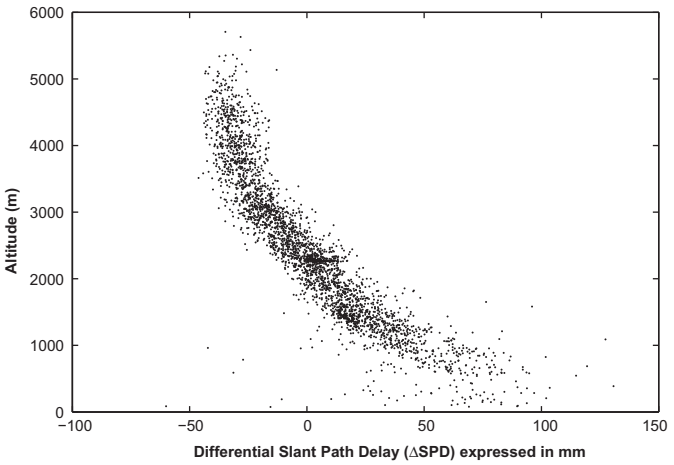

Fig. 6. Example of altitude dependence of ΔSPD calculated for two randomly selected images. The systematic variation can be reasonably well approximated by a cubic spline. Nevertheless, it is notable that at lower elevation the relation between ΔSPD and topography is less well defined. This is mainly due to horizontal variation of the PWV along the coast.

discriminate ground displacement contributions from the atmospheric signal. The availability of global PWV measurements since the launch of satellite solar spectrometers provided evidence of more complex behavior and offers alternative approaches for reducing atmospheric effects.

Because the vertical stratification of water vapor is effectively arbitrary, there is no physically based model for the differential delay induced by atmospheric water vapor. As such, the elevation dependent part of ΔSPD must be modeled as an arbitrary function with sufficient degrees of freedom to correctly represent the mean vertical structure, but not so many as to allow the function to be fit to non-topographic variation. Based on visual inspection of a large sample of MODIS images, we found that a generalized fourth order spline with 4 knots provided a realistic, reliable and robust representation of the vertical variation of ΔSPD in the Atacama region. Fig. 5a' and b' show maps of the median and 95th percentile of the residual ΔSPD after removal of the topographic dependence using a four order spline model. Again, the 95th percentile can be taken as a pessimistic view of the residual atmospheric phase contribution after the application of the proposed strategies. These maps reveal that the approach is a useful way to mitigate tropospheric contribution from interferometric signals on the study area. The ΔSPD is significantly reduced on the high plateau area which features numerous strato volcanoes. On the other hand, the simplicity of the chosen model, which does not take horizontal in-homogeneity of the PWV field into account, retains significant atmospheric phase delay residuals over the coastal area where large subduction earthquake occur. We will discuss further the consequences of such effects on InSAR mapping of crustal deformation and on the accuracy of earthquake source parameters inverted from InSAR data.

4. Discussion

The understanding of many aspects of the earthquake cycle observed in northern Chile has recently increased through model parameter estimations derived from InSAR data analysis. InSAR data have also provided improvement for the estimations of fault parameters (geometry and location) in earthquake studies, as well as for spatial variation of fault slip (e.g., Pritchard et al., 2002; Chlieh, 2003; Pritchard and Simons, 2006). These studies also showed that numerous sources of errors can significantly affect the

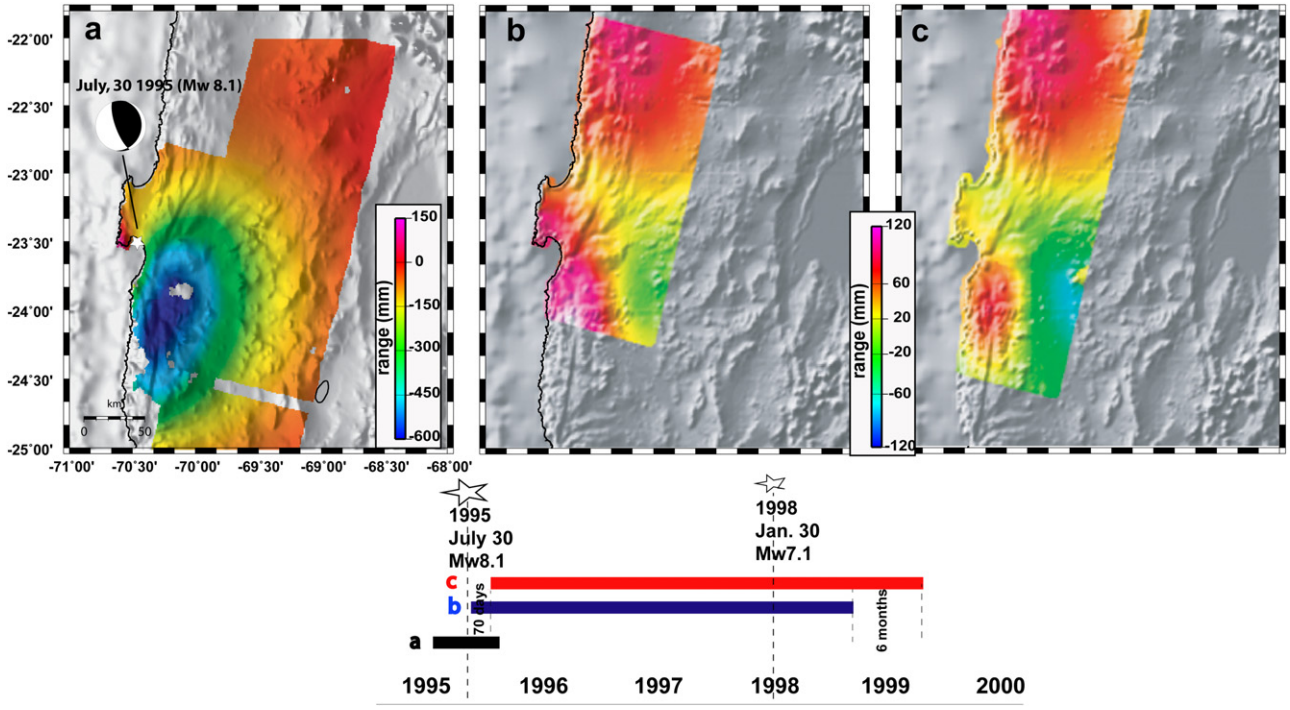

Fig. 7. Example of three unwrapped interferograms computed over the study area. a) Unwrapped interferograms spanning the 1995 Mw = 8.1 Antofagasta subduction earthquake. Unwrapped post 1995 M.w 8.1 Antofagasta earthquake interferograms beginning b) 6 h c) 71 days after the earthquake. The difference between both post-seismic interferograms mostly concerns the background signal in the southern area. As the interferogram in b includes the radar image acquired 6 h after the earthquake, the postseimic ground deformation signal would be stronger than in the interferogram shown in c but the spatial pattern in both interferograms would be similar. Nevertheless, strong atmospheric artifacts blur the post-seismic signal in the interferogram shown in c.

accuracy of the geophysical parameters deduced by InSAR. Pritchard et al. (2007) showed that change in velocity model, the fault parameterization (e.g. number, size and dip of subfaults), the inversion strategy (e.g. weighting of a smoothing operator) can impact geodetic moment by 10% or larger. Atmospheric phase delays can also lead to biased model parameter estimates or/and to difficulties in interpreting deformation events captured with InSAR. The analysis of our large database of MODIS image gave evidence that phase delays variations may exceptionally exceed 100 mm and more typically reach about 20 mm and that the vertical variation of water vapor induced path delay dominates the spatial pattern. The amplitude of atmospheric effects in the study area are so much less than the coseismic deformation from earthquakes with magnitude >7 such as those occurred in 1995 and 1998 (tens of centimeters). Nevertheless, these effects can lead to difficulties in interpreting deformation events captured with InSAR.

The Mw 8.1 Antofagasta earthquake of July 30, 1995 was the largest subduction earthquake that occurred in northern Chile in the XXth century and has been extensively studied from seismic data and geodetic (InSAR and GPS) measurements (Ruegg et al., 1996; Delouis et al., 1997; Klotz et al., 1999; Pritchard et al., 2002; Chlieh et al., 2004). The unwrapped interferograms of this earthquake indicate major crustal deformation that reaches up to 600 mm of increasing range change in the LOS of the ERS-radar (Fig. 7). The 1995 Antofagasta earthquake was followed in January 30, 1998 by the Mw = 7.1 earthquake. Two unwrapped interferograms of this event were computed using two ERS-radar passes separated respectively by 3.6 years (Pair 1, 7b) and 3.3 years (pair 2, 7c). Pair 1 starts 6 h after the 1995 main shock and therefore includes most of the post-seismic deformation. Pair 2 starts 70 days after the earthquake. Both interferograms exhibit two different displacement patterns separated by the Mejillones Peninsula. The signal covering the north of the Peninsula is similar in both pairs and was interpreted as interseismic loading (Chlieh et al., 2004). South of the Mejillones Peninsula, the signal is composed of an uplift (decreasing range) flanked far inland by a subsidence (increasing range) with a gradient of about 120 mm in Pair 1 and about 100 mm in Pair 2. This signal was interpreted as a superposition of the coseismic deformation of the 1998 Mw = 7.1 earthquake (contribution of 60% of the total signal) and post-seismic deformation that follows the 1995 Mw = 8.1 Antofagasta earthquake (Pritchard and Simons, 2002; Chlieh et al., 2004). One discrepancy that appears between pair 1 and pair 2 was a persistent shift between the two signals of about 40 mm that could not be explained by any consistent tectonic model. Chlieh (2003) suggested that moisture which is often trapped within local topographic depression of the Salar del Carmen and the Salar de Navidad could explain such effects (see also Section 3.3 and Fig. 5). The persistent shift observed between pair 1 and pair 2 interferograms falls in the range of the atmospheric phase delays measured in this study (20–100 mm) and then the atmospheric phase delay may be a consistent explanation to reconcile the discrepancy that appeared between pair 1 and pair 2 interferograms.

In the remainder of the paper, we will focus on the impact of these atmospheric phase delays on the determination of two fundamental earthquake source parameters: (i) the geodetic moment and (ii) the slip distribution on the coseismic fault plane deduced from single interferograms analysis. We will thus evaluate the potential and the effectiveness of atmospheric filtering based on the tropospheric delay-elevation relationship. In order to prescribe the magnitude of atmospheric delay errors we used 1000 randomly selected images of ΔSPD (described previously in Section 3.3). We applied this approach to the analysis of the fault rupture and slip distribution of the 1995 Mw = 8.1 Antofagasta earthquake.

4.1. Uncertainty analysis of geodetic moment estimation

The seismic moment is a classical quantity used in seismology to measure the size of an earthquake and is derived from seismic observations (short and long period). With the advent of geodetic instruments (GPS and InSAR), the source of an earthquake could be determined from the inversion of geodetic data, and the moment associated is called the geodetic moment. Its expression (M_0) is given by $M_0 = \mu S \Delta u$, where μ is the shear modulus of the medium involved in the earthquake, S is the area of the rupture along the geologic fault and Δu is the average displacement within the fault area. The assessment of the atmosphere-induced uncertainties of the estimated geodetic moment derived from InSAR observations can be undertaken by inverting the series of ΔSPD images. Thus ΔSPD data are here considered as deformation signal and inverted. As for surface displacements induced by fault dislocation, each ΔSPD surface field is modeled using a single dislocation within a homogeneous elastic half space (Okada, 1992). The fault parameters are fixed using the values proposed by Delouis et al. (1997) except the slip which is set to be free. The inversion then yields the error of the slip displacement related to tropospheric signals observed by MODIS and then the error on the geodetic moment estimation. The result of this simple approach indicates that the variability of the atmospheric phase screen in the study area leads to a median absolute error of 12 cm and a standard deviation of 24 cm in the determination of the slip displacement deduced from InSAR measurements. This could trigger an error up to 3.3×10^{27} dyn cm at a 95% confidence level in the determination of the seismic moment of the 1995 July 30 Mw = 8.1 Antofagasta earthquake. Pritchard et al. (2002) proposed a geodetic moment of 24×10^{27} dyn cm. This result shows that tropospheric signal could induce a bias of about 10% on the inferred slip displacement for an earthquake of magnitude Mw = 8 deduced from InSAR data.

As vertical stratification is dominant in the study area, we applied the same strategy as described above, but using as input data our set of ΔSPD images with the elevation dependant part removed. This simple approach significantly reduces the error in the determination of the fault slip magnitude: the median error is reduced to about 1 cm with a standard deviation of 2 cm and the error in the determination of the geodetic moment is reduced to 1.3×10^{26} dyn cm at a 95% confidence level.

4.2. Uncertainty analysis of the slip distribution estimation

Although uniform slip models can provides useful information (in particular concerning the geometry of the fault plane), it is well known that homogeneous slip along the fault plane is not physically reasonable. InSAR data provides dense and accurate measurements of the deformation field which makes it possible to determine the distribution of slip along the fault plane. To further explore the accuracy of InSAR-derived model for the earthquake, we now focus more precisely on the impact of atmospheric signal in the determination of the coseismic slip distribution along the fault plane. We thus fixed the geometry and the discretization of the fault plane into patches using the fault plane model for the Mw 8.1 Antofagasta earthquake proposed by (Pritchard et al., 2002). We decided to fix the rake angle to 113°, which is the mean value found by the authors for the fault patches with the best constrained slip. By fixing the geometry, the inversion for the amplitude of the slip becomes linear and is given by the equation $\mathbf{Gm} = \mathbf{d}$, where $\mathbf{m}$ is a vector of the amplitude of the slip on each patch, $\mathbf{d}$ is the vector of the induced tropospheric phase delays and $\mathbf{G}$ is the matrix of Green functions for each fault patch computed using an isotropic elastic half-space model (Okada, 1992). We use a least-square constrained linear inversion (CLS) which is part of the MATLAB Optimization

Toolbox (Gill et al., 1991) to resolve the slip distribution. We evaluated the robustness of the approach as follows. We generated synthetic data corresponding to null displacements, adding an uncorrelated Gaussian noise with standard deviation of 50 mm and then inverting the synthetic data for the fault slip. The maximum resulting error for the slip is about 20 mm.

Fig. 8a shows a typical example of ΔSPD field induced by water vapor temporal variation observed in the study area. This ΔSPD field map gives a relative measure of ΔSPD with respect to a reference point located the Andean Cordillera at 4000 m of altitude, for which the variations of PWV are minimal. It reveals a spatial pattern of ΔSPD with as high as 50 mm of differential delays between the coast and the Andean Cordillera. As commonly observed (see Fig. 5), fine scale ΔSPD patterns are observed, roughly centered on the Salar of Navidad, Salar del Carmen and on Mejillones Peninsula. Both the amplitude and the spatial pattern have an important impact on the inferred slip values which prevents the determination of an accurate slip distribution. The amplitude of the fault slip induced by tropospheric effects is significant and can reach up to 60 cm as shown in Fig. 8b. Obviously modeled data are also largely biased by these effects (Fig. 8c).

By removing the elevation dependant part in the ΔSPD values, the atmospheric contribution is significantly reduced over a large area as showed in Fig. 8a'. The best fitting delays explain 52% of the variance observed. Nevertheless, the large horizontal variability of PWV along the coast leads to higher residuals along the coastal strip and on the relief close to the sea (up to 10 mm) than those observed on the high plateau area. As the elevation dependent model cannot take fine-scale ΔSPD patterns observed along the coast into account, this leads to an overestimation of the amplitudes of modeled ΔSPD. In spite of this intrinsic limit, this approach enables reduction of errors in the slip distribution as evidenced in Fig. 8b' and c'.

A more detailed analysis using our set of 1000 randomly selected image pairs confirms the efficiency of elevation dependent

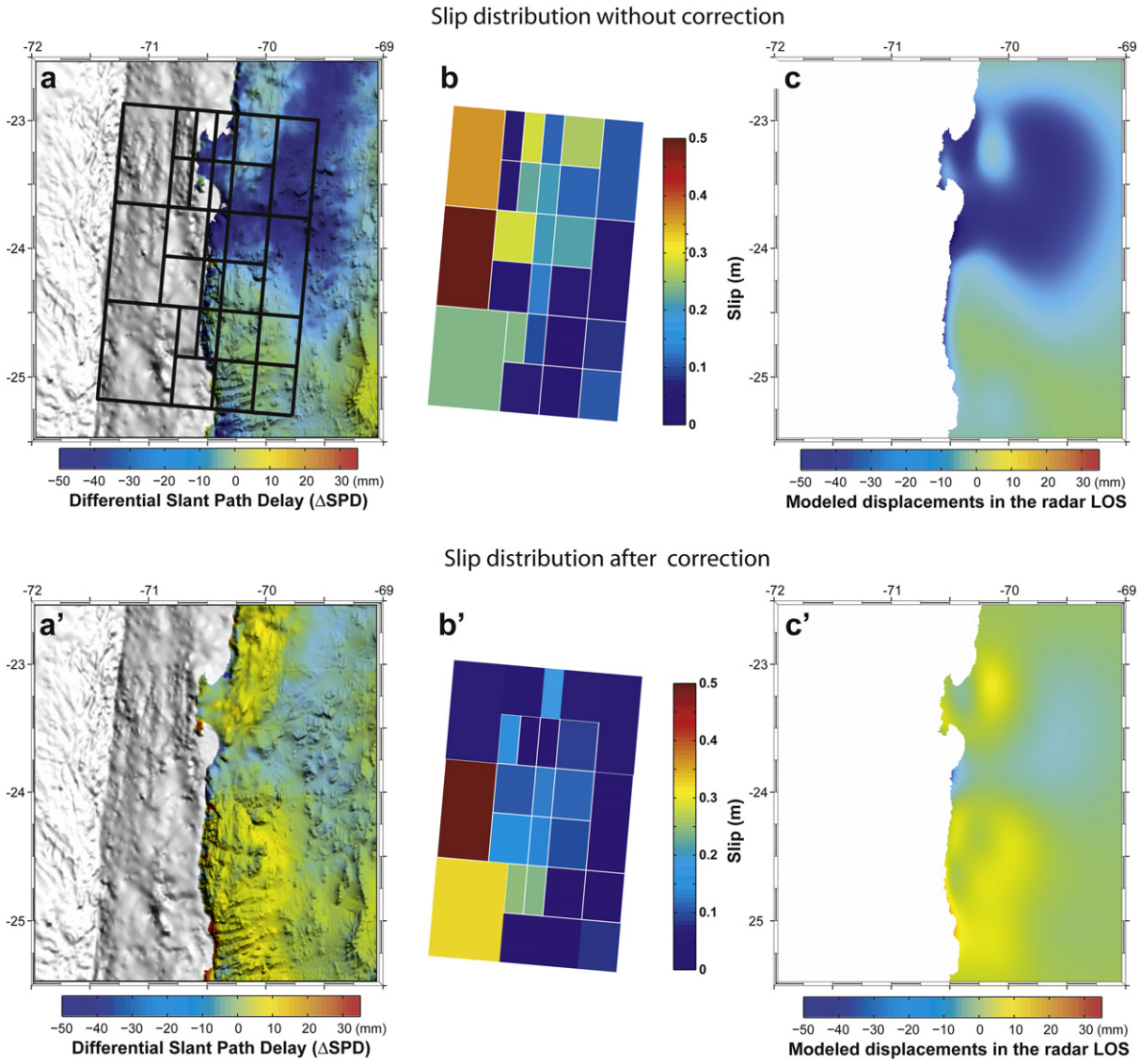

Fig. 8. a) Typical example of ΔSPD field observed in the study area. The black rectangles show the fault plane divided in 26 patches used by (Pritchard et al., 2002) for analyzing the 1995 July 30 Mw = 8.1 Antofagasta earthquake. b) Slip distribution from constrained least square method using as data in input the ΔSPD field showed in A. The induced magnitude of slip induced by tropospheric effects can reach up to 0.60 m in this example. c) Predicted interferogram for inversion using the ΔSPD data as input. a') The same field as in a but after removing the elevation dependence of ΔSPD (52% of the variance observed in a). b') Slip distribution from constrained least square method using as data in input the ΔSPD field showed in a'. The uncertainties in the determination of the slip distribution are generally well reduced except for slips near the trench, which are poorly resolved using measurements acquired on land. c') Predicted interferogram for inversion using the corrected ΔSPD as input.

model to reduce uncertainties in the determination of the slip distribution. This analysis also emphasizes the limitation of such an approach. Fig. 9 gives the absolute value of the median error on the determination of each patch slop deduced from the CLS inversions of the set of 1000 randomly selected image pairs without (9a) or after removal of the elevation dependent part (9a') and their 95% confidence intervals (9b and 9b'). We obtain median absolute errors ranging between about 0.10 and 0.40 m and 0.05–0.20 m without or after removal of the elevation dependent part in the ΔSPD values, respectively. In both cases the confidence intervals are large (9b, 9b') and indicate the high variability of the noise structure from one SPD image to other related to atmospheric heterogeneities in the study area. Even though the elevation dependent model reduces the uncertainties in the determination of the slip distribution, they remain high.Two main reasons explain these high uncertainties. The one is that not all the fault patch are equally well resolved because MODIS data, in the same way as InSAR data, are limited to be on land and therefore the slip distribution is poorly resolved offshore. Furthermore, the variation of tropospheric delays induced by the horizontal variability of the atmosphere, which is not taken into account in our approach, could seriously limits the precision of two pass interferometry data to determine accurate fault slips distribution for a big earthquake.

4.3. Potential of multi-temporal InSAR methods

The analysis of the realistic atmospheric noise upon inversion of geophysical parameter presented above provides an incomplete picture because it only involves the analysis of single interferograms. Promising results have instead been proven by using multi-image information (Ferretti et al., 2001; Berardino et al., 2002; Usai, 2003; Simons and Rosen, 2007). The most common approach consists of reducing the contribution of the atmospheric phase delays by averaging several independent SAR interferograms (Simons and Rosen, 2007). Stacking in general degrades the temporal resolution of InSAR measurements and this approach makes it difficult to detect short-lived transient displacements but it is a very good approach to study earthquake or deformation process approximately linear in time. This method is a reliable approach to minimize atmospheric contamination as it can reduce the variance of atmospheric error by a factor of N (where N is the number of independent interferograms).

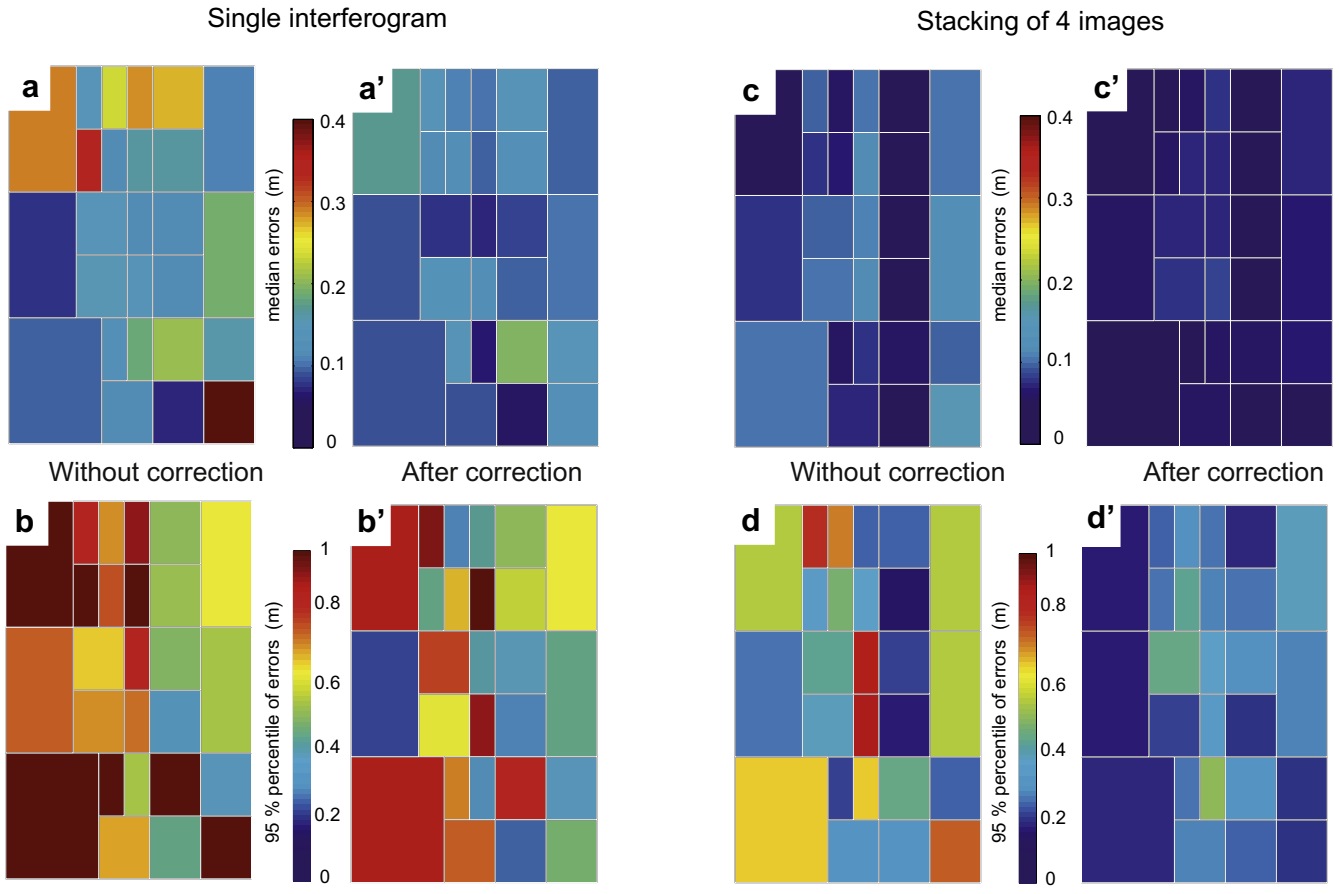

Fig. 9. Error estimations of the slip distribution related to tropospheric effects. (aa'–bb') Error estimations of the slip distribution related to tropospheric effects using a single interferograms. They are computed from the CLS inversion of the set of 1000 randomly selected image pairs. Each ΔSPD image is considered as a synthetic interferograms. a and a' show absolute values of the median slip distribution without or after removal of the elevation dependant part in the ΔSPD fields, respectively. b and b' show the 95% confidence intervals of the slip distribution obtained before and after removed the elevation dependant part in the ΔSPD fields, respectively. The uncertainties in the determination of the slip distribution are generally reduced after removal the elevation dependant part in each ΔSPD image. Nevertheless, they remain high due to patches poorly resolved offshore and by the horizontal variability of the atmosphere. Figure cc'–dd' show error estimations of the slip distribution related to tropospheric effects using a stack of 4 independent interferograms. They are computed from the CLS inversion of the set of 500 randomly stacks of 4 image pairs. Each ΔSPD image is considered as a synthetic interferograms. c and c' show the absolute values of the median slip distribution without or after removal of the elevation dependant part in the ΔSPD images used in the stacks, respectively. d and d' show the 95% confidence intervals of the slip distribution obtained before and after removed the elevation dependant part in the ΔSPD images used in the stacks, respectively. The uncertainties in the determination of the slip distribution are well reduced after removal the elevation dependant part in each ΔSPD image. Note that a different color scale is used between Figure [a–a',c–c'] and Figure [b–b',d–d'] in order to better contrast the different uncertainty maps.

In order to assess the efficiently of the stacking approach to mitigate atmospheric errors, we make use of the database of 1000 randomly selected image pairs of ΔSPD to create a set of 500 stacks of 4 independent ΔSPD images. Fig. 9c and d shows the absolute values of the median slip distribution and the 95% confidence intervals computed from the CLS inversion of this set of data. This confirms a well known result that using interferograms acquired on several different dates well minimizes atmospheric contamination and significantly reduce the uncertainties in the determination of the slip distribution estimated by the inversion technique.

The analysis of our large database of MODIS image reveals that correlated component due to vertical-stratified water vapour distribution often dominates and represents a large part of the InSAR atmospheric phase variability in the study area. Thus, in order to assess the impact of topographically correlated atmospheric path delays in the inference of fault slip using a stacking approach, we inverted again the same dataset but after removing the topographic dependence in each ΔSPD image (9c' and 9d'). Visual comparison between results 9c–c' and 9d–d' clearly shows that this sample correction applied leads to better results in the determination of the slip distribution along the fault plane. Using such a similar approach, allowed Pritchard et al (2006) (by selecting a subset of interferograms stacked them together) to detect a ~1 cm LOS signal for the April 19, 1996 earthquake in northern Chile.

It should be stressed also that another particularly effective way to investigate the spatial and temporal evolution of ground motion is through interferometry time series. When multi-temporal dataset is available, two main methodologies could be used to monitor deformation of the Earth's surface: the permanent scattered (Ferretti et al., 2001) and the short baseline time series approach (SBAS) (Berardino et al., 2002; Usai, 2003). Both approaches basically involve the analysis of a long stack of SAR images. In earthquake cycle, most of the elastic strain accumulated at the plate interface of the subduction zone accumulated during decades or centuries is released suddenly (few seconds or minutes) in a large earthquake and its aftershocks. So this is a main shortcoming of these methods as a large number of SAR images are needed to get reliable result. However these approaches could give useful results to survey long duration displacements induced by several processes of energy release accompanying large earthquake such as inter or post-seismic deformation, for instance. In these approaches the atmospheric artifacts are identified through a two-step filtering operation which is based on the correlation of the atmosphere in space and its decorrelation in time. For example, in SBAS approach the atmosphere phase component is detected as the result of the cascade of a low-pass filtering step, performed in the two-dimensional spatial domain (i.e., azimuth and range) and a high-pass filtering operation with respect to the time variable. We now focus on the impact of correlated atmospheric path delays to the InSAR measurements time series computed via the SBAS algorithm.

To analyze this impact, we select 50 MODIS images acquired on the study area, which sample the period 2003 to 2009. The uneven sampling of MODIS data is next converted in single path propagation delays using the Eq. (1) with respect to a reference point located in the Salar of Atacama. Based upon the large variability of PWV at the Mejillones Peninsula shown previously (see Fig. 5), we follow the temporal evolution of the single path propagation delays at a point inside the peninsula.

Fig. 10a shows the resulting time series of single path propagation delays for this selected point. The variability of PWV induces large amplitude dispersion in the data distribution and a fluctuation of about 100 mm in peak to peak amplitude. The temporal time series composed of 50 irregularly spaced samples is then smoothed by using a Bartlett window of a length 300 days. The resulting smoothed time series could be directly compared with the unsmoothed one. Vertical variation of PWV induced path delay is effectively reduced to peak to peak amplitude of about 30 mm. Nevertheless, this implies the ground motion retrieved after temporal smoothing could be affected by an error of about 30 mm in LOS between the coast and the cordillera. So residual tropospheric signal remains in smoothed InSAR time series and could seriously blur signal related to slow deformation events such those produced by post or interseimic processes. Next we apply the same strategy as described above but after removing the elevation dependant part in the time series. The efficiently of the approach is validated by the decrease in data dispersion in both unsmoothed and smoothed time series (Fig. 10b). The smoothed signal has now peak to peak amplitude of about 5 mm.

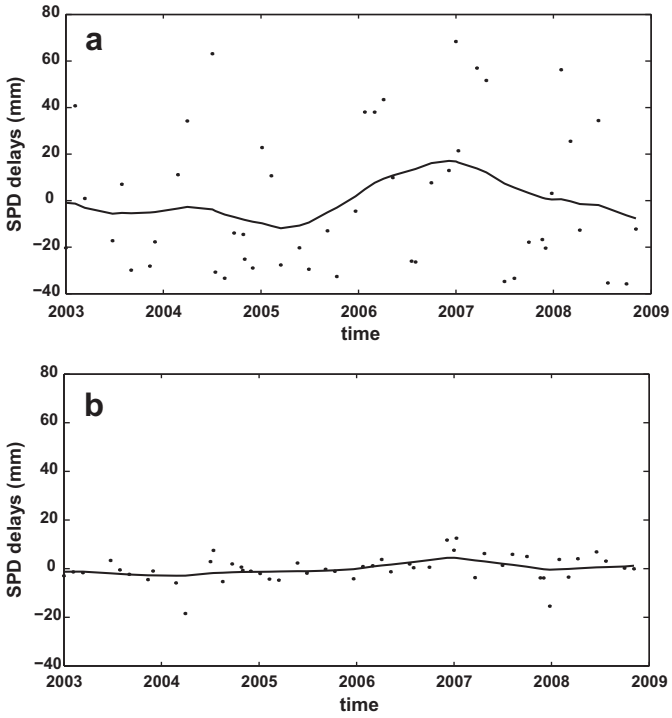

Fig. 10. Two-way SAR slant path signal delays induced by atmospheric water vapor sampled at Mejillones Peninsula (see Fig. 5). a). SPD plot here are estimated from a five-year sample of 50 MODIS images and are expressed in respect with a reference point located in the Salar of Atacama. This figure illustrates the high variability of water along the Chilean coast. The solid line shows the resulting smoothed time series using a Bartlett window of 300 days length. The temporal fluctuations in the smoothed time series are about 30 mm in peak to peak amplitude. Consequently, in this case the ground motion retrieved from uncorrected interferograms using multi-temporal approach would be affected by an error of about 30 mm in LOS between the coast and the Andean Cordillera. Obviously, it is possible to reduce this amplitude by increasing the filter width. Nevertheless, such an option would also blur both transient and slow ground motions related to tectonic activity in the same way. b) The same time series as in a but after removing the elevation dependence. The temporal fluctuations of the signal are clearly reduced and the smoothed one has now peak to peak amplitude of about 5 mm. By comparing a and b it is possible to quantify how topographically correlated atmospheric path delay is effectively removed by smoothing and the importance to correct such a delay before employing a smoothing approach.

Hence, we conclude that topographically correlated atmospheric path delays must be estimated and corrected, if possible, in each interferogram before employing stacking or smoothing approaches in such a way to better mitigate tropospheric phase delay.

5. Conclusions

Mapping the spatial distribution of fault slip is essential to better understand the mechanisms of the earthquake processes and the mechanical behavior of the upper layers of the Earth. The spatial

distribution and quantification of seismic and/or aseismic slip along the subduction zone and consequently the degree of inter-plate seismic coupling at the plate interface parallel to the trench has important implications for evaluating the potential of neighboring fault to generate future earthquakes. Due to the low density of ground based monitoring networks in most part of the Chilean subduction margin, InSAR is the main alternative for geodesists to produce the most accurate maps of the Earth's surface displacement related to subduction processes. The scope of this paper was to give a quantitative understanding of the impact of atmospheric noise upon the estimation of the distribution of fault slip and geodetic moment by InSAR. Our main conclusions could be summarized as follows:

(i) The comparison between MODIS and GPS derived PWV estimations in northern Chile shows that both estimates are in good agreement. The mean standard deviation of 1.3 mm compares well with similar statistics presented in previous studies (Li, 2004). Consequently, over a large part of northern Chile no external calibration of MODIS data is necessary and PWV estimates show promise as an independent means of estimating the atmospheric component in InSAR images collected in this area.

(ii) The analysis of a one-year database of MODIS image allowed us to characterize both the pattern and the amplitude of expected tropospheric signal in SAR interferograms on the Salar de Atacama region from elevations between 0 to over 5000 m. It reveals that the vertical variation of water vapor induced path delay dominates the spatial pattern in the study area. This analysis also reveals that phase delay variations usually reach about 20 mm in the study area and in exceptional cases can reach up to 100 mm. Such effects could be comparable in magnitude and wavelength with surface displacements produced by typical subduction earthquake of moderate magnitude (shallow Mw ~6 or deep Mw ~7 earthquake) or post-seismic deformation that follows large Mw ~8 earthquake.

(iii) Our result shows that tropospheric signal could induce a bias of about 10% on the inferred slip displacement deduced from InSAR data for an earthquake of magnitude Mw = 8 in the study area. PWV induced path delay can affect the accuracy of the geophysical parameters deduced by inversion of InSAR data in the same order of magnitude than other errors sources such as change in velocity model, fault parameterization (e.g. number, size, dip of subfaults) or inversion strategy.

(iv) Our study shows that the effectiveness of the stacking or SBAS techniques is improved when a traditional atmospheric filtering based on the tropospheric delay-elevation relationship is used to reduce the dispersion in time series of InSAR measurements. This result, in agreement with other studies (Peyrat et al., 2006; Pritchard and Simons, 2006; Cavalié et al., 2008; Elliott et al., 2008; Doin et al., 2009), confirms that even using time series of SAR images, topography correlated atmospheric delays must be estimated and corrected, if necessary.

(v) Even if it could be possible to estimate topography correlated tropospheric effects directly from the interferograms, this method has a disadvantage in that any geodynamical signals correlated with topography in the same way will be removed. In this context, satellite based PWV estimates offer a reliable alternative means to discriminate displacement contributions from the atmospheric signal.

Our approach in this paper has not provided a ready-made solution to mitigate the tropospheric contribution in InSAR data but rather has quantified their consequences in the context of earthquake studies. Atmospheric effects remain one of the limiting error sources in the use of InSAR techniques and further works are still necessary to develop more effective methods to mitigate their effects in geophysical studies.

Acknowledgments

We wish to thank M. Pritchard for his useful comments and his encouragement. We thank ENTEL Chile (Iquique), Dirección General de Aeronáutica Civil de Chile (Iquique), Mineria Dona Ines de Collahuasi, Universidad Arturo Prat, Sernageomin Iquique for the logistic support for the northern Chile GPS network. The GPS data were acquired in the frame of the French-Chilean cooperation program by IRD, IPG Paris and Department of Geophysics and the Seismological Service of the University of Chile. The MERIS and ENVISAT data have been acquired through ESA research projects: ENVISAT A-O n°857 (PI: JL. Froger) and Category 1 research project N°2899 (PI: S. Bonvalot). This study has been supported by IRD (Dept. DME, DSF), University of Chile (Department of Geophysics/Meteorology) and ECOS-CONICYT (project n°C00U03) FONDECYT-CONICYT (project n° 1030800) and IRD-CONICYT.

References

Beauducel, F., Briole, P., Froger, J.L., 2000. Volcano wide fringes in ERS synthetic aperture radar interferograms of Etna (1992-1999): deformation or tropospheric effect? Journal of Geophysical Research 105, 16391–16402.

Bennartz, R., Fischer, J., 2001. Retrieval of columnar water vapour over land from backscattered solar radiation using the medium resolution imaging spectrometer. Remote Sensing of Environment 78, 274–283.

Berardino, P., Fornaro, G., Lanari, R., Sansosti, E., 2002. A new algorithm for surface deformation monitoring based on small baseline differential SAR interferograms. Geoscience and Remote Sensing, IEEE Transactions on *40*, 2375–2383.

Bevis, M., Businger, S., Chiswell, S., Herring, A.T., Anthes, R.A., Rocken, C., Ware, R.H., 1994. GPS Meteorology: mapping zenith wet delays onto precipitable water. Journal of Applied Metereology 33, 379–386.

Bevis, M., Chiswell, S., Businger, S., Herring, T.A., Bock, Y., 1996. Estimating wet delay using numerical weather analysis and predictions. Radio Science 31, 447–487.

Cavalié, O., Doin, M.-P., Lasserre, C., Briole, P., 2007. Ground motion measurement in the Lake Mead area, Nevada, by differential synthetic aperture radar interferometry time series analysis: probing the lithosphere rheological structure. Journal of Geophysical Research 112.

Cavalié, O., Lasserre, C., Doin, M.-P., Peltzer, G., Sun, J., Xu, X., Shen, Z.-K., 2008. Measurement of interseismic strain across the Haiyuan fault (Gansu, China), by InSAR. Earth and Planetary Science Letters 275, 246–257.

Chlieh, M., 2003. Le Cycle Sismique décrit avec les données de la Géodésie Spatiale (interférométrie SAR et GPS différentiel): variations spatio-temporelles des glissements stables et instables sur l'interface de subduction du Nord Chili. In: Géophysique Interne. Institut de Physique du Globe de Paris, p. 173.

Chlieh, M., de Chabalier, J.B., Ruegg, J.C., Armijo, R., Dmowska, R., Campos, J., Feigl, K., 2004. Crustal deformation and fault slip during the seismic cycle in the North Chile subduction zone, from GPS and InSAR observations. Geophysical Journal International 158, 695–711.

Delacourt, C., Briole, P., Achache, J., 1998. Tropospheric corrections of SAR interferograms with strong topography. Application to Etna. Geophysical Research Letters 25, 2849–2852.

Delouis, B., Monfret, T., Dorbath, L., Pardo, M., Rivera, L., Compte, D., Haessler, H., Caminade, J.P., Ponce, L., Kausel, E., Cisternas, A., 1997. The Mw 8.0 Antofagasta (Northern Chile) earthquake of 30 July 1995: a precursor to the end of the large 1877 gap. Bulletin of the Seismological Society of America 87, 427–445.

Doin, M.P., Lasserre, C., Peltzer, G., Cavalié, O., Doubre, C., 2009. Corrections of stratified tropospheric delays in SAR interferometry: validation with global atmospheric models. Journal of Applied Geophysics, in press, [Corrected proof].

Elliott, J.R., Biggs, J., Parsons, B., Wright, T.J., 2008. InSAR slip rate determination on the Altyn Tagh Fault, northern Tibet, in the presence of topographically correlated atmospheric delays. Geophysical Research Letters 35.

Falvey, M., Garraud, R., 2005. Moisture variability over the South American Altiplano during the SALLJEX observing season. Journal of Geophysical Research 110. doi:10.1029/2005JD006152.

Ferretti, A., Prati, C., Rocca, F., 2001. Permanent Scattered in SAR interferometry. IEEE Transactions on Geoscience and Remote Sensing 39, 8–20.

Froger, J.L., Remy, D., Bonvalot, S., Legrand, D., 2007. Two Scales of inflation at Lastarria-Cordon del Azufre volcanic complex, central Andes, revaled from ASAR-ENVISAT interferometric data. Earth and Planetery Science Letters. doi:10.1016/j.epsl.2006.12.012.

Gao, B.-C., Kaufman, Y.J., 2003. Water vapor retrieval using Moderate Resolution Imaging Spectroradiometer (MODIS) near-infrared channels. Journal of Geophysical Research D13. doi:10.1029/2002JD003023.

Garreaud, R.D., 1999. A multi-scale analysis of the summertime precipitation over the central Andes. Monthly Weather Review 127, 901–921.
Gill, P.E., Murray, W., Wright, M.H., 1991. Practical Optimisation. Academic Press, London.
Hanssen, R., 2001. Radar Interferometry Data Interpretation and Errors Analysis. Kluwer Academic Publishers, Dordrecht, The Netherland.
Herring, A.T., King, R.W., McClusky, S.C., 2006a. GPS Analysis at MIT, Gamit Reference Manual, Release 10.3. Massachussetts: M.I.T, Cambridge.
Herring, T.A., King, R.W., McClusky, S., 2006b. Global Kalman Filter VLBI and GPS Analysis Program, Globk Reference Manual, Release 10.3. Massachussetts: M.I.T, Cambridge.
Klotz, J., Angermann, D., Michel, G.W., Porth, R., Reigber, C., Reinking, J., Viramonte, J., Perdomo, R., Rios, V.H., Barrientos, S., Barriga, R., Cifuentes, O., 1999. GPS-derived deformation of the central Andes including the 1995 Antofagasta Mw = 8.0 earthquake. Pure and Applied Geophysics 154, 709–730.
Li, Z., Muller, J.P., Cross, P., 2003. Comparison of precipitable water vapor derived from radiosonde, GPS and Moderate-resolution Imaging Spectroradiometer measurements. Journal of Geophysical Research 108. doi:10.1029/2003JF=D003372.
Li, Z., 2004. Production of Regional 1 km × 1 km Water Vapor Fileds through the Integration of GPS and MODIS Data. ION gnss. Inst. of Navig, Long Beach Californie. 21–24 Sept.
Loveless, J.P., Pritchard, M.E., 2008. Motion on upper-plate faults during subduction zone earthquakes: case of the Atacama Fault System, northern Chile. Geochemistry, Geophysics, Geosystems 9, Q12017.
Okada, Y., 1992. Internal deformation due to shear and tensile faults in a half-space. Bulletin of the Seismological Society of America 82, 1018–1040.
Pavez, A., Remy, D., Bonvalot, S., Diament, M., Gabalda, G., Froger, J.L., Julien, P., Legrand, D., Moisset, D., 2006. Insight into ground deformation at lascar volcano (Chile) from SAR interferometry, photogrammetry and GPS data: implication on volcano dynamics and future space monitoring. Remote Sensing of Environment 100, 307–320.
Perfettini, H., Avouac, J.-P., Ruegg, J.-C., 2005. Geodetic displacements and aftershocks following the 2001 Mw = 8.4 Peru earthquake: implications for the mechanics of the earthquake cycle along subduction zones. Geophysical Journal International 110.
Peyrat, S., Campos, E., de Chabalier, J.B., Perez, A., Bonvalot, S., Bouin, M.-P., Legrand, D., Nercessian, A., Charade, O., Patau, G., Clevede, E., Kausel, E., Bernard, P., Vilotte, J.-P., 2006. The Tarapaca intermediate-depth earthquake (Mw 7.7, 2005, Northern Chile): a slab-pull event with horizontal fault plane constrained from seismologic and geodetic observations. Geophysical Research Letters 33. doi:10.1029/2006GL027710.
Pritchard, M.E., Simons, M., 2002. A satellite geodetic survey of large scale deformation of volcanic centres in the central Andes. Nature 418, 167–170.
Pritchard, M.E., Simons, M., Rosen, P.A., Hensley, S., Webb, F.H., 2002. CO-seismic slip from the 1995 July 30 Mw=8.1 Antofagasta, Chile, earthquake as constrained by InSAR and GPS obervations. Geophys. J. Int 150, 362–376.
Pritchard, M.E., Simons, M., 2006. An aseismic slip pulse in Northern Chile and along-strike variation in seismogenic behavior. Journal of Geophysical Research 111. doi:10.1029/2006JB004258.
Pritchard, M.E., Norabuena, E.O., Ji, C., Boroschek, R., Comte, D., Simons, M., Dixon, T.H., Rosen, P.A., 2007. Geodetic, teleseismic, and strong motion constraints on slip from recent southern Peru subduction zone earthquakes. Journal of Geophysical Research 112.
Puysségur, B., Michel, R., Avouac, J.P., 2007. Tropospheric phase delay in interferometric synthetic aperture radar estimated from meteorological model and multispectral imagery. Journal of Geophysical Research 112.
Remy, D., Bonvalot, S., Briole, P., Murakami, M., 2003. Accurate measurement of tropospheric effects in volcanic area from SAR interferometry data: application to Sakurajima volcano (Japan). Earth and Planetery Science Letters 213, 299–310.
Ruegg, J.C., Campos, J., Armijo, R., Barrientos, S., Briole, P., Thiele, R., Arancibia, M., Cañuta, J., Duquesnoy, T., Chang, M., Lazo, D., Lyon-Caen, H., Ortlieb, L., Rossignol, J., Serrurier, L., 1996. The M_w = 8.1 Antofagasta (North Chile) earthquake of July 30, 1995: first results from teleseismic and geodetic data. Geophysical Research Letters 23, 917–920.
Rutllant, J.A., Fuenzalida, H., Aceituno, P., 2003. Climate dynamics along the arid northern coast of Chile: the 1997-1998 Dinámica del Clima de la Region de Antofagasta (DICLIMA) experiment. Journal of Geophysical Research 108, 002003. doi:10.1029/2002JD003357.
Simons, M., Rosen, P., 2007. Treatise on Geophysics, interferometric synthetic aperture radar Geodesy. In: Schubert, G.E. (Ed.), Geodesy. Elsevier Press, pp. 391–446.
Tregoning, P., Boers, R., Obrien, D., Hendy, M., 1998. Accuracy of absolute precipitable water vapor estimates from GPS observations. Journal of Geophysical Research 103, 28701–28710.
Usai, S., 2003. A least squares database approach for SAR interferometric data. Geoscience and Remote Sensing, IEEE Transactions on 41, 753–760.
Zebker, H.A., Rosen, P.A., Heinsley, S., 1997. Atmospheric effects in interferometric synthetic aperture radar surface deformation and topographic maps. Journal of Geophysical Research 102, 7547–7563.